International Journal of Fatigue 199 (2025) 109059

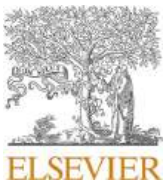

Contents lists available at ScienceDirect

International Journal of Fatigue

journal homepage: www.elsevier.com/locate/ijfatigue

The effect of corrosion on the fatigue crack-growth of 17-4 PH stainless steel specimens made by selective laser melting☆

America Califano [a,*], Enrico Armentani [b], Filippo Berto [c], Raffaele Sepe [a]

[a] Department of Industrial Engineering, University of Salerno, Via Giovanni Paolo II 132, 84084 Fisciano, Italy
[b] Department of Chemical, Material and Industrial Production, University of Naples Federico II, P.le V. Tecchio 80, 80125 Naples, Italy
[c] Department of Chemical Engineering, Materials, Environment, Sapienza University of Rome, Rome, Italy

ARTICLE INFO

Keywords:
Fatigue-crack-growth
Fracture
17-4 PH
Additive manufacturing
Corrosion

ABSTRACT

The numerous advantages of the Selective Laser Melting (SLM) technology have made it a quite common Additive Manufacturing (AM) process for components made in metals and metallic alloys. Several factors, like building direction, defects, residual stresses and corrosion can substantially jeopardize the performance of the finished products obtained with such manufacturing process. In this regard, the present study investigates the impact of corrosion on the fatigue crack-growth behavior of 17-4 PH stainless steel specimens manufactured through SLM. This type of stainless steel, known for its high strength and corrosion resistance, is widely used in applications requiring durability under cyclic loading. For this reason, this work explores how the experimental crack initiation and propagation rates are affected by two cross different orientations of the initial notch (horizontal and vertical), different testing environments (air and seawater) and different load frequencies. Findings also highlight how corrosion accelerates fatigue crack growth in SLM-fabricated specimens, indicating a need for tailored post-processing treatments to enhance their performance in corrosive environments.

1. Introduction

Understanding the fatigue crack growth (FCG) phenomenon in engineering materials is essential for ensuring the structural integrity, reliability, and longevity of components, particularly those subjected to cyclic loading. Predicting and modeling FCG is, however, inherently complex due to the stochastic nature of fatigue processes, which are influenced by a multitude of interdependent variables, including material microstructure, environmental conditions, and applied stress profiles [1]. Among commonly used engineering materials, stainless steels are particularly valued for their excellent corrosion resistance and mechanical resilience, making them indispensable in various industrial applications, from aerospace and marine to energy and medical sectors. Stainless steels' robustness under both static and dynamic loading conditions is further enhanced by their alloying elements, which improve their capacity to withstand aggressive environmental factors while maintaining their structural properties over extended periods.

One high-performing alloy, 17-4 PH stainless steel (SS), is widely recognized for its exceptional mechanical properties, attributed to a martensitic microstructure strengthened through precipitation hardening. This alloy's unique combination of properties, including high strength, hardness, and corrosion resistance, renders it suitable for critical applications where both mechanical load-bearing and corrosion resistance are required [2]. The alloy's microstructural and chemical composition plays a pivotal role in its response to fatigue-induced cracking and corrosion. Microstructural features, such as grain size, phase distribution, and the presence of strengthening precipitates, directly impact how cracks initiate and propagate under cyclic loading. Indeed, FCG in materials like 17-4 PH SS is influenced not only by mechanical loading but also by external environmental factors such as exposure to corrosive media, temperature fluctuations, and pH levels. In particular, the presence of seawater or other corrosive environments is known to accelerate crack growth in steels by promoting crack initiation and propagation [3].

In recent years, Additive Manufacturing (AM) technologies have transformed the landscape of materials engineering and component production. Various stainless-steel alloys, including 17-4 PH, are now being processed through AM methods, such as Selective Laser Melting (SLM) [4]. These techniques allow for highly flexible design capabilities, enabling the creation of complex geometries and significantly reducing

☆ This article is part of a special issue entitled: 'Fatigue CP 2024' published in International Journal of Fatigue.

* Corresponding author.
E-mail address: amcalifano@unisa.it (A. Califano).

https://doi.org/10.1016/j.ijfatigue.2025.109059
Received 28 February 2025; Received in revised form 19 April 2025; Accepted 11 May 2025
Available online 12 May 2025

the production lead times, which is especially advantageous for custom or small-batch components [5,6]. At the same time, mechanical properties and microstructure of parts made by additive manufacturing are influenced by many factors, first and foremost the manufacturing process [7–10] and the testing conditions [11–13]. AM components often exhibit distinct microstructural features, such as columnar grains, increased porosity, and residual stresses, which can influence their mechanical behaviour and fatigue life under real-world service conditions. Given that many applications of stainless steel involve exposure to corrosive environments [14], understanding the corrosion fatigue crack growth behaviour of AM 17-4 PH SS has become an area of growing research interest.

Experimental studies have shown that fatigue performance under corrosive conditions – such as in saline solutions, acidic media, or environments with high humidity – results in a notable decrease in the fatigue life of AM 17-4 PH SS compared to its performance in ambient air [15]. This happens because of the corrosive environment that accelerates crack initiation and growth [16], particularly at the material's surface and in regions with microstructural inhomogeneities, such as pores, inclusions, or grain boundaries [17–19]. For instance, Stoudt *et al.* [20] conducted potentiodynamic scans to evaluate the electrochemical behaviour of AM 17-4 PH SS in a deaerated 0.5 mol/l NaCl solution, attributing its relatively high corrosion resistance to a refined martensitic lath structure that forms during the AM process. Syrett *et al.* [21] studied the corrosion fatigue performance of this alloy in the presence of a 6 % FeCl3 corrosive solution and found that fatigue life was significantly reduced in such aggressive environments, with fatigue performance showing dependency on loading frequency. Their findings revealed that as the load frequency decreased from 50 Hz to 12 Hz, the fatigue life of the alloy diminished, highlighting the role of both mechanical and environmental factors in driving FCG.

More in general, the corrosion fatigue behaviour of AM 17-4 PH stainless steel is complex and influenced by many aspects such as microstructural features, surface finish, heat treatment, and build orientation during the AM process [22,23]. While AM technology offers substantial advantages in design flexibility and manufacturing efficiency, these benefits are offset by challenges related to process-induced defects and unique microstructural characteristics, which can compromise corrosion fatigue performance. Current research suggests that surface irregularities and microstructural discontinuities serve as critical sites for crack initiation under cyclic loading, with crack propagation driven by complex interactions between applied mechanical stresses and corrosive processes like pitting [24]. For example, Schönbauer et al. [25] investigated the influence of corrosion pits on the fatigue life of turbine blades made of 17-4 PH steel, observing that an increase in pit size was correlated with a significant reduction in corrosion fatigue life. Such findings underscore the importance of controlling surface and microstructural quality to enhance fatigue resistance, especially in harsh environments.

In this paper, the influence of corrosion fatigue and frequency of fatigue load on crack growth of the specimens made in 17-4 PH SS by Selective Laser Melting (SLM) has been studied. The specimens underwent detailed metallographic analysis, were instrumented, and subsequently tested under controlled conditions. Fatigue crack-growth tests were performed in both air and corrosive environments, by means of a custom-designed testing apparatus, with varying load frequencies, to assess the combined effects of environmental exposure and mechanical loading (Section 2). Then, the microstructure of the specimens, the crack-growth curves and the corrosion curves obtained downstream of the experiments were discussed and final observations were provided about the key findings of the present study were provided (Section 3 and Section 4).

2. Materials and methods

2.1. Specimens preparation

The commercial EOS GP1 (UNS S17400) powder was used as raw material and its chemical composition, reported in Table 1, is within specification of the composition of martensitic precipitation hardening 17-4 PH stainless steel. A rectangular plate, with sizes 170 × 70 × 7 mm × mm × mm was manufactured by SLM, setting the printing parameters optimized for this purpose and listed in Table 2, according to [26] and choosing the *z*-axis as building direction, see Fig. 1. After that, the plate was milled until the final sizes 168 × 68 × 6.65 mm × mm × mm were obtained (Fig. 1A), and ten specimens [23,27] with dimensions reported in Fig. 1B, were extracted by using the Electric Discharge Machining (EDM) machine. One sample was used for metallographic and corrosion analyses and nine C(T) specimens were used for crack-growth tests: specimens n. 2, 3, 5 and 8 were tested in air, whereas specimens n. 1, 4, 6, 7 and 9 were tested under corrosion, namely in artificial seawater. As visible in Fig. 1, specimens n. 1, 2, 3, 6 and 7 had the notch parallel to the *y* direction (identified as "horizontal" notch, H), while specimens n. 4, 5, 8 and 9 had the notch parallel to the *x* direction (identified as "vertical" notch, V).

2.2. Metallographic analysis

Half of specimen n. 10 was used to carry out a surface metallographic analysis in order to investigate the effect of the manufacturing process on the material's macrostructure. The sample, after being embedded in the resin, was grinded and polished by using diamond suspension solution. The microstructures were observed by means of light microscope after the etching that was obtained by using the Vilella reagent, consisting of 1 g of picric acid, 5 ml of hydrochloric acid and 100 ml of ethanol.

2.3. Corrosive solution preparation

Five crack propagation tests under corrosion were carried out keeping the specimens soaked in a corrosive environment. The solution consisted in an in-house artificial marine water solution, which was obtained following the ASTM D1141-98 Standard [29]. The solution was prepared by stirring 2 l of deionised water with the required amounts of salts listed in Table 3.

The suitable salt quantities were weighted using a KERN ABJ 120-4NM analytical balance and dissolved in deionised water by means of a FALC magnetic stir. Afterwards, by adding some drops of a 0.1 M solution of sodium hydroxide (NaOH) and using an XS pH7 pH-meter, the solution pH was adjusted to 8.00, for obtaining a basic marine water solution.

2.4. Corrosion testing

Corrosion tests were performed following the ASTM 647 standard [30]. During this kind of test, the sample was kept soaked for thirty minutes in the testing environment for measuring the Open-Circuit Potential (OCP) [32]. Then, starting from the OCP, a ramp with a rate of 1 mV every six seconds was applied. As customary for this kind of experiment, the test was stopped when the pitting corrosion was sensibly appreciable, namely when the colour of the solution changed due to the accumulation of iron ions.

2.5. Crack propagation tests

Fatigue crack propagation tests were performed on C(T) specimens by fatigue tension–tension tests, according to the ASTM 647 standard [30] by means of an Instron 8502 testing machine equipped with a load cell of 20 kN. The applied fatigue load had a maximum load, P_{max}, =

Table 1
Chemical composition of nitrogen atomized 17-4 stainless steel powders in wt % [28].

C	Cr	Ni	Cu	Mn	Si_{max}	Mo	Nb	Fe
≤ 0.07	15 ÷ 17	3 ÷ 5	3 ÷ 5	≤ 1	≤ 1	≤ 0.5	0.15 ÷ 0.45	Balance

Table 2
Printing parameters used for manufacturing.

Parameter	Value
Operating laser power [W]	195
Operating wavelength [nm]	1030
Linear scanning speed [m•s^{-1}]	1.2
Hatch distance [mm]	0.09
Layer thickness [μm]	20
Focused laser diameter [μm]	90

4500 N and a loading ratio, $R = 0.1$. All specimens were pre-cracked with a load frequency of 5 Hz until a 1.3 mm long crack was reached (total crack length a of 6.38 mm, hence $a/W = 0.251$); afterwards, for the specimens tested in corrosion environment, the frequency was reduced in order to evaluate the corrosion effect on the crack growth rate [29].

Three values of frequency after pre-cracking were considered:

i) $f = 0.5$ Hz for specimens n. 4 and 6;
ii) $f = 1$ Hz for specimens n. 7 and 9;
iii) $f = 2.5$ Hz for specimen n. 1.

A summary of the tested specimens is reported in Table 4.

An *ad-hoc* equipment was manufactured for keeping the specimens immersed in the marine water solution during the experimental tests. The system consisted in a Polytetrafluoroethylene (PTFE) box, a pump and a tank, and it was mounted on the mechanical testing machine through dedicated screws (Fig. 2A). The tank was used to store the solution at atmospheric pressure and was connected to the box with two rubber tubes. The inlet and outlet tubes allowed to keep the sea water solution continuously circulating during tests for avoiding the precipitation of salts in the solution and, thus, encouraging the oxidation phenomenon. A detail of the specimen and the box mounted onto the machine is shown in Fig. 2B. With reference to tests in corrosion solution, before carrying the fatigue crack propagation tests, each specimen was immersed for 24 h in the corrosive solution so as to promote the effects of corrosion on the material itself; afterwards, the specimens were mounted onto the grips of the testing machine and the pumping system was turned on in such a way to fill the PTFE box.

During the corrosion-fatigue crack propagation tests, the specimen was immersed in seawater and therefore it was impossible to access it. Thus, the Back-Face Strain (BFS) technique was used to track the crack growth during the tests [22,23,31]. This technique was developed for crack-growth tests on C(T) specimens and is based on correlation of the strain at the back face of the specimen with the crack length in the

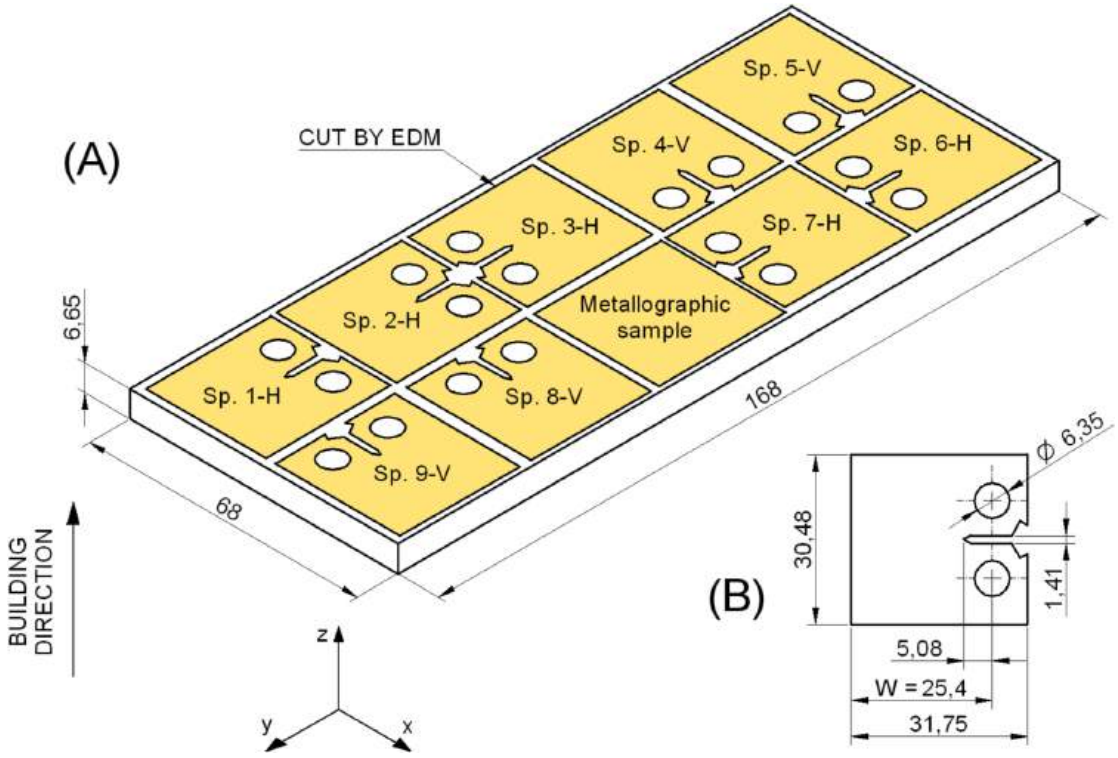

Fig. 1. (A) Milled printed plate with the main dimensions and the position of the specimens, (B) dimensions of specimens.

Table 3
Salts for 1 l of deionised water, according to ASTM D1141-98.

Compound	NaCl	$MgCl_2$	Na_2SO_4	$CaCl_2$	KCl	$NaHCO_3$	KBr	H_3BO_3	$SrCl_2$	NaF
Concentration [g/l]	24.53	5.20	4.09	1.16	0.695	0.201	0.101	0.027	0.025	0.003

Table 4
Testing conditions for all specimens.

Specimen	Environment	Pre-cracking freq. [Hz]	Testing freq. after pre-cracking [Hz]	Notch orientation
1	Seawater	5.0	2.5	H
2	Air	5.0	5.0	H
3	Air	5.0	5.0	H
4	Seawater	5.0	0.5	V
5	Air	5.0	5.0	V
6	Seawater	5.0	0.5	H
7	Seawater	5.0	1.0	H
8	Air	5.0	5.0	V
9	Seawater	5.0	1.0	V

specimen itself. This approach is similar to the compliance measurement technique, in which the crack length is estimated using the crack mouth displacement. As in the compliance measurement, in which the load, the material and the crack mouth displacement are correlated to the crack length, also for the BFS technique the strain values measured by a strain gauge attached at the back face of the specimen (at mid-height and mid-width, see Fig. 3) are correlated to the instantaneous crack length. The correlation between BFS data and crack length was obtained by calibration curves developed in air for a given loading condition and, then, was used also for tests in seawater.

Therefore, each specimen was equipped with a CEA 06-032UW-120 strain-gauge of Vishay Intertechnology ® at the back-face (back-face strain-gauge, BFS, see Fig. 3A) and protected against seawater corrosion by applying a silicone-rubber coating on it (see Fig. 2B). Those tested in

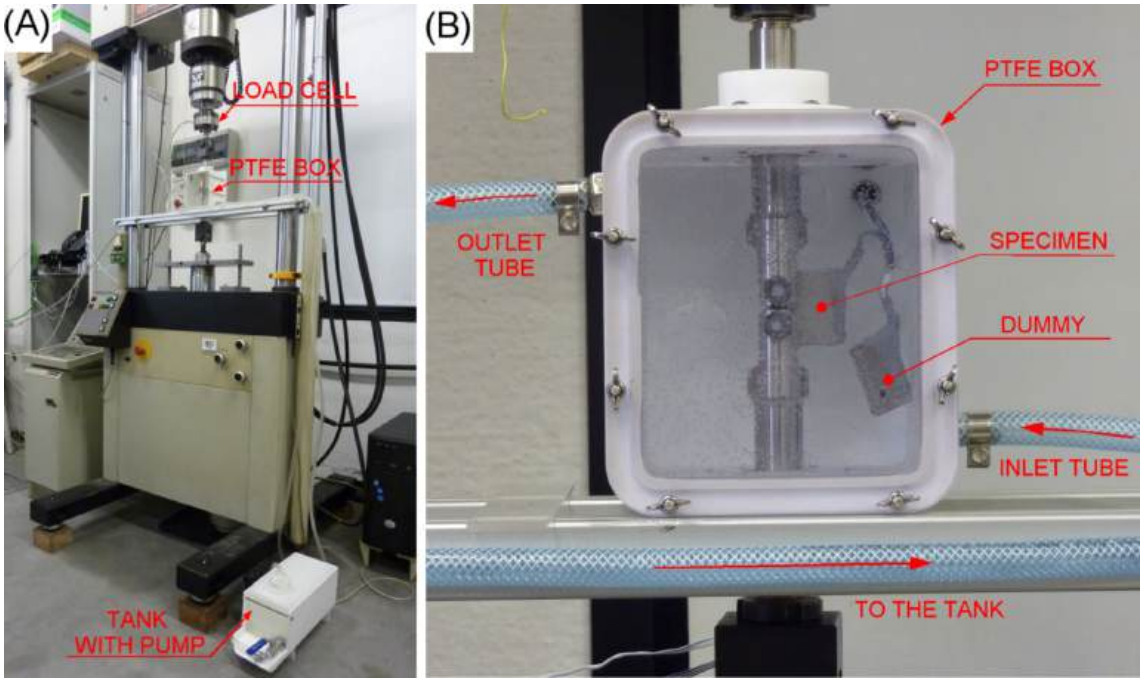

Fig. 2. (A) Layout of the testing machine with the device for corrosion fatigue test; (B) Detail of the PTFE box and the specimen mounted into the *ad hoc* manufactured testing device.

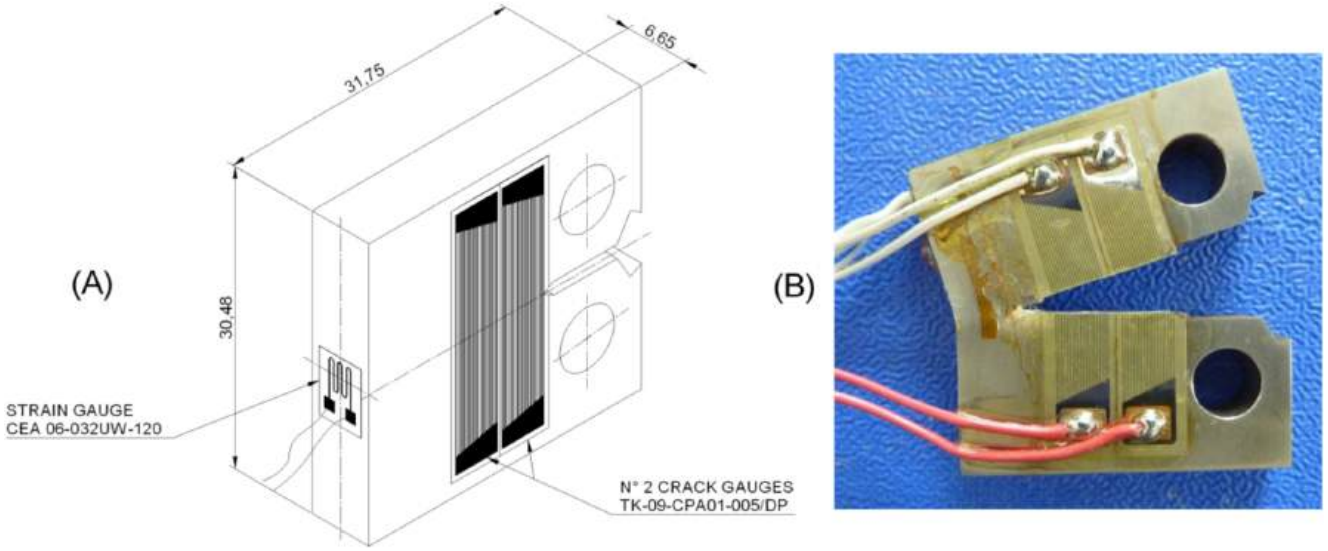

Fig. 3. (A) C(T) specimen equipped with a strain gauge and two crack gauges; (B) C(T) specimen instrumented at end of test.

air were also additionally equipped with two Crack-Gauges (CG) TK-09-CPA01-005/DP of Vishay Intertechnology ® glued at one side (Fig. 3). Each CG presented 20 filaments with a mutual distance of 0.254 mm (similarly to [22,23,31]).

The BFS values and length of crack, *a*, measured by crack gauges were recorded with a National Instruments instrumentation at a frequency of 150 Hz and, then, they were extracted and post-processed. The BSF values were converted in a crack length *a* according the Newman-Johnston approach available in literature [31] and that will be presented afterwards.

Four calibration tests were performed; two for each notch direction (see Fig. 1A).

For all tests in seawater environment, a "dummy" specimen equipped with a CEA 06-032UW-120 strain gauge was also left in the box (see right side of Fig. 2B) so as to record the strain data caused by room temperature variations during the day. This strain data was subtracted to the BFS one acquired with the loaded specimen, in order to increase the measurement accuracy of the mechanical strain. The C(T) specimens were subjected to fatigue tests up to total failure. Afterwards, the fracture surfaces of some specimen were analysed by Scanning Electron Microscope (SEM).

3. Results and discussion

This section presents the key findings of the study, focusing on the primary outcomes and trends observed in the experimental evidence. First of all, the microstructure of the specimens was analyzed and then the results coming from the corrosion tests were discussed. Finally, the data of the crack propagation tests were presented, comparing the outcomes of the experiments carried out in air with those carried out in the corrosive environment.

3.1. Metallographic analysis

A metallographic analysis was performed for investigating the effect of the build direction on the microstructure profile. The macrographs for the three coordinated planes (*xy*, *yz* and *xz*), defined through the coordinate system of (Fig. 1), are reported in Fig. 4. Generally, for materials made by SLM samples, there are important differences in the microstructure, depending on the orientation of the surface. Fig. 4A and 4B show the microstructure in the plane *xy* perpendicular to building direction. The laser scanning path with circular patterns is visible, indicating the SLM process profiles, in accordance with literature [32]. Moreover, it is possible to observe that there are some lack of fusion defects (or unmelted regions), which can be attributed to low laser penetration depth. These types of defects are slit-shaped pores with small volume, but that can cover a wide region.

Fig. 4C-4F show the microstructure in the *xz* and *yz* planes respectively that is more heterogeneous if compared to that of the *xy* plane. Columnar grains (indicated by black arrows Fig. 4E) and lath martensite are present. In fact, during the manufacturing process, the heat, generated by the current scanning the layer to sinter the powder, flows towards the previously solidified layers (*i.e.* parallel to the build direction) thus encouraging the epitaxial grain growth mechanism [33]. Accordingly, grains elongate towards the build plate and become columnar. These grains may have a length of hundreds of microns and, indeed, may extend over several layers of powder. This means that during the molten pool solidification, the freshly formed crystals, while growing, adopt the orientation of the lower previously formed grains. It should be noted that depending on the input energy, the molten pool may include a part or the entire previous layer [34,35]. Consequently, this is the reason for the large-size grains inside the metal material, especially in the building direction.

In Fig. 4C (in *xz* plane) the hemispherical melt pools with an average width of 110 μm and average depth of 20 μm are evident, which corresponds to the hatching distance and layer thickness used during the manufacturing process, respectively.

Fig. 4D and 4F show the presence of both martensitic and austenitic phases in the samples. Although fully-martensitic material can be expected at equilibrium for this alloy [36], retained austenite "islands" were homogeneously formed within the boundaries of martensite grains.

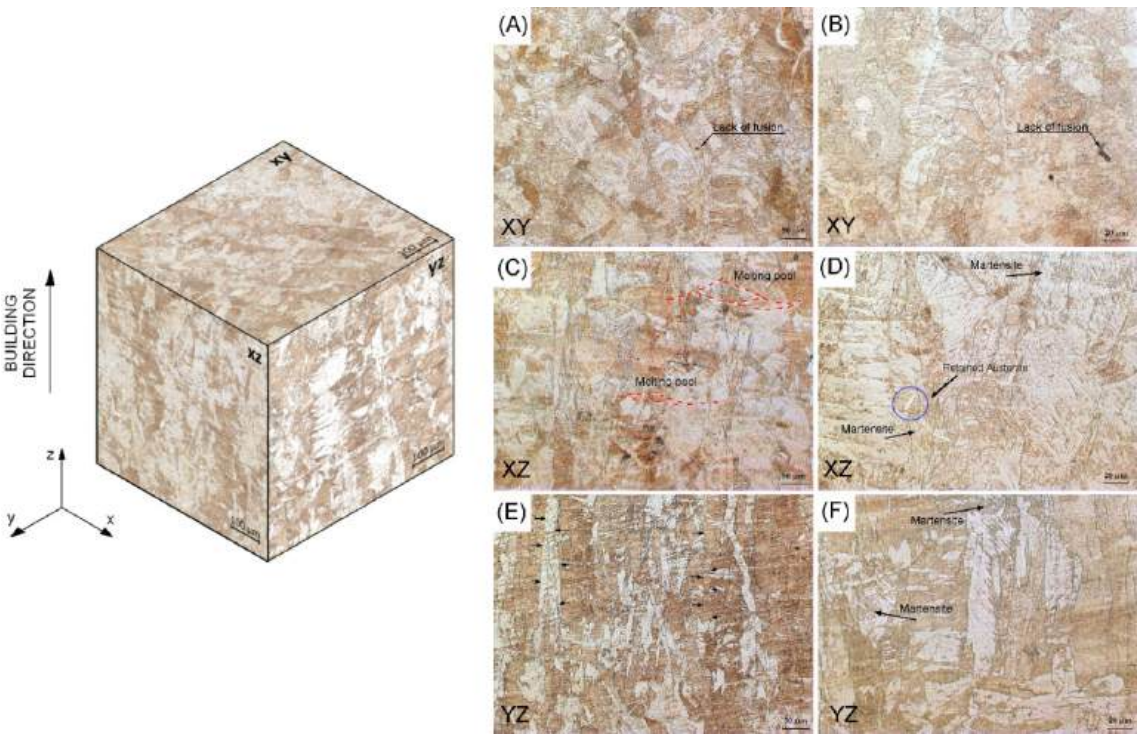

Fig. 4. Microstructure of material on the three different planes.

The presence of the retained austenite depends on chemical composition of powder and nitrogen content. In fact, the concentrations of the alloying element, such as Cr, Ni, and Cu, among others, can impact on both solidification and solid-state phase transformations during cooling, instead it is well established that nitrogen has the ability to stabilize austenite at low temperature [37,38]. Usually, the metallurgical evolution of 17-4 PH stainless steel is the following: under equilibrium cooling condition, it solidifies as primary delta-ferrite from liquid stat; after that, the delta-ferrite phase transforms to austenite due to the solid-state diffusion and, finally, the austenite transforms to martensite in range of 160 °C until room temperature is reached [37,39–41]. This solidification mechanism can be influenced from concentrations of the alloying element and nitrogen content and the impact of the changes of these can be evaluated by the ratio of Cr and Ni equivalent values (Cr_{eq} and Ni_{eq}). The higher Cr_{eq}/Ni_{eq} ratio, the higher the stability of ferrite/martensite. The lower this ratio, the higher stability of austenite.

The Cr_{eq} and Ni_{eq} values can be calculated by means Eqs. (1) and (2) [37]:

$$Ni_{eq}\ (wt\%) = [Ni] + 30\ [C] + 30\ [N] + 0.5\ [Mn] \quad (1)$$

$$Cr_{eq}\ (wt\%) = [Cr] + [Mo] + 1.5\ [Si] + 0.5\ [Nb] \quad (2)$$

A Cr_{eq}/Ni_{eq} ratio higher than 1.5, implies that the first solidification phase is ferrite and then a full martensitic microstructure at the end of cooling, but this value can increase with increasing the cooling rate. From literature [37,40–42] it can be acquired that the nitrogen atomized powder presents a lower value of Cr_{eq}/Ni_{eq} ratio and, therefore, the microstructure of AM samples, made with GP1 powder, can present retained austenite with different fractions of the austenite itself [20,36,42,43].

3.2. Corrosion test

The Open Circuit Potential (OCP) curve of the 17-4 PH stainless steel specimens tested in seawater is shown in Fig. 5.

The OCP curve provides critical insights into the electrochemical stability and corrosion resistance of this material. As a matter of fact, the OCP measurement involves monitoring the potential of a metal electrode relative to a reference electrode in the absence of an external current (*i.e.*, under open circuit conditions). This passive measurement helps in understanding the thermodynamic tendency of the metal to corrode in a specific environment. From Fig. 5 it can be noticed that the OCP shows some fluctuations, witnessing an active corrosion process and/or changes in the passive film's properties. This happens because initially, upon immersion, the potential may fluctuate as the system reaches equilibrium. Eventually, it stabilizes to a steady-state potential, which reflects the balance between anodic and cathodic reactions on the material surface in seawater. Potentiodynamic (PD) polarization curve is shown in Fig. 6. All the tested samples represent a typical behaviour for a passive metal, including a typical active–passive transition region and a passivation region.

In particular, in the cathodic region (negative potentials) the curve represents reactions such as oxygen reduction; for seawater, the cathodic reaction is often dominated by the reduction of dissolved oxygen. The anodic region (positive potentials) indicates the dissolution of iron from the steel, represented by a significant increase in current density. The presence of a passivation region depends on the formation of a protective oxide film. The width and stability of this passive region can be affected by the chloride ions in seawater, which tend to destabilize the passive film, causing pitting corrosion. Potentiodynamic polarization testing involves sweeping the electrode potential at a constant rate and recording the resulting current density. This method provides detailed information on various electrochemical parameters, including corrosion potential (E_{corr}), corrosion current density (i_{corr}), passivation behaviour, and pitting susceptibility. In this case, it was computed that E_{corr} is −0.253 V, while the Tafel constants are −0.205 (anodic slope) and −0.308 (cathodic slope), respectively, and the i_{corr} is $1.05{\cdot}10^{-7}$ A/cm^2. These values are comparable with those found in literature [2,44,45] for 17-4 PH stainless steels manufactured by SLM, witnessing the reliability of the manufacturing process.

3.3. Crack propagation tests

The aim of this work is evaluating the influence of corrosion with different values of frequency of applied loading on crack growth rate of the specimens in 17-4 PH stainless steels made by SLM.

As anticipated, to evaluate the crack length *a*, during the tests, a BFS technique was adopted. Briefly, the so-called Newman-Johnston equations [31] are useful for monitoring the crack-length-against-cycles, valid for the standard C(T) specimens, and can be applied to a wide range of crack-length-to-width ratios. The main equation of the approach is the following:

$$\frac{a}{W} = A_0 + A_1 U + A_2 U^2 + A_3 U^3 + A_4 U^4 + A_5 U^5 \quad (3)$$

where:

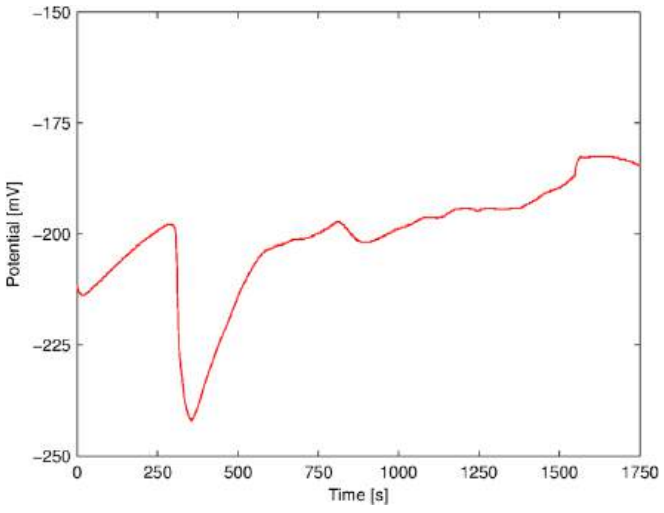

Fig. 5. Open Circuit Potential (OCP) curve of the 17-4 PH stainless steel specimens tested in seawater.

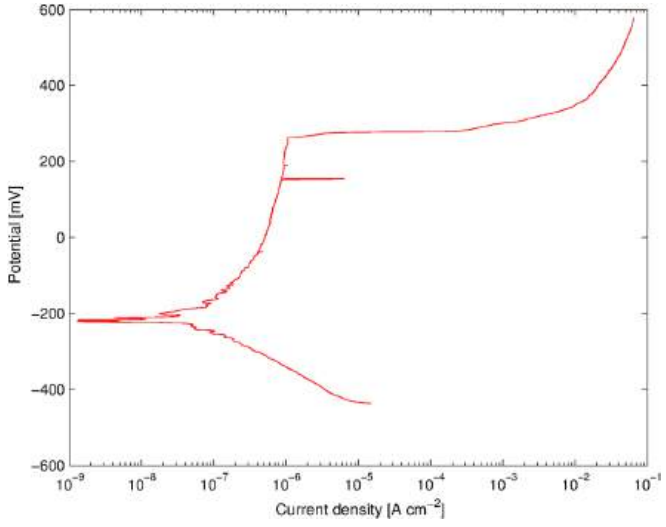

Fig. 6. Potentiodynamic (PD) polarization curve for the 17-4 PH stainless steel specimen tested in seawater.

$A_0 = 1.0343$, $A_1 = -2.8098$, $A_2 = 4.1335$, $A_3 = -23.694$, $A_4 = 76.371$, $A_5 = -83.25$ for $0.2 < a/W < 0.8$ [31];

$$U = \frac{1}{(\sqrt{A}+1)} \tag{4}$$

$$A = \left| E(\varepsilon \bullet W)\frac{B}{P} \right| \tag{5}$$

where:

E is the Young modulus, ε is the mechanical strain measured by the BFS, $W = 25.4$ mm, $B = 6.65$ mm and $P = P_{max} = 4500$ N. Therefore, before carrying out the crack propagation tests in seawater solution, a calibration procedure for BFS technique had to be performed, comparing data collected by the BFS and the CG, in order to evaluate the value of the Young modulus, E, to be introduced in eq. (5).

In detail, specimens n. 2 and 3, with the notch parallel to the y direction, and n. 5 and 8, with the notch parallel to the x direction (see Fig. 1A), equipped with a BFS and a CG were tested in air; the data collected through the BFS and the CG were cross-compared for calibration by means of the Newman-Johnston equations (1) – (3) [31]. At end of the calibration procedure, $E = 165$ GPa of the tested material was found for all specimens. This result can be considered in accordance with literature where, typically, a Young modulus of about 180 GPa was found [46].

Fig. 7A and 7B show the data collected through the BFS and the CG in terms of crack length, a, *vs.* number of cycles, N, for specimen n. 2 and n. 5, respectively, tested in air. The black curve represents the crack length measured by the BFS, while the red squares represent the crack length data obtained through the CG during the experiments in air.

3.3.1. Crack propagation tests in air environment

Fig. 8 shows the *a-N* curve for specimens tested in air with different orientations of the notch. Cycle counting started after a pre-cracking phase that consisted in discarding the first 1.3 mm of propagation. Therefore, the cycle counting started at an initial crack length, a, of about 6.38 mm. Pure Mode-I fracture was observed for all specimens, according to the test setup.

From Fig. 8, it can be noticed that the four specimens showed a similar mechanical behaviour, thus highlighting a good repeatability. As a matter of fact, although the specimens have the notch oriented differently in the original AM plate (see Fig. 1), the notches belonged to the same plane, thus sharing the same microstructure. Hence, the crack-growth behaviour was not significantly influenced by the crack orientation, at least for those considered in this work.

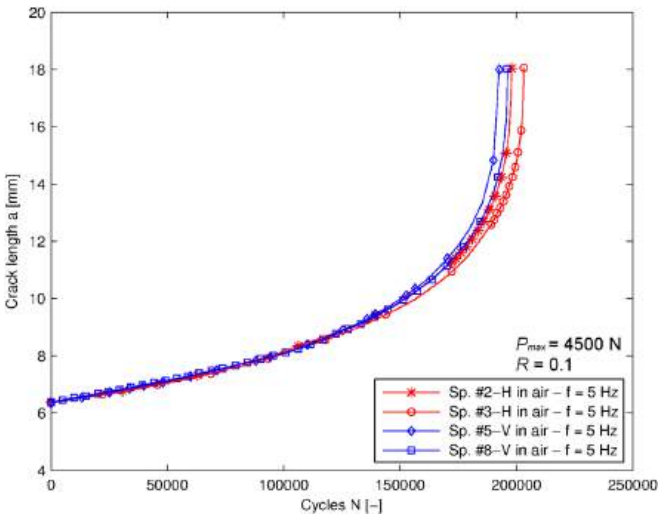

Fig. 8. *a-N* curves for different direction of notch orientation in air environment.

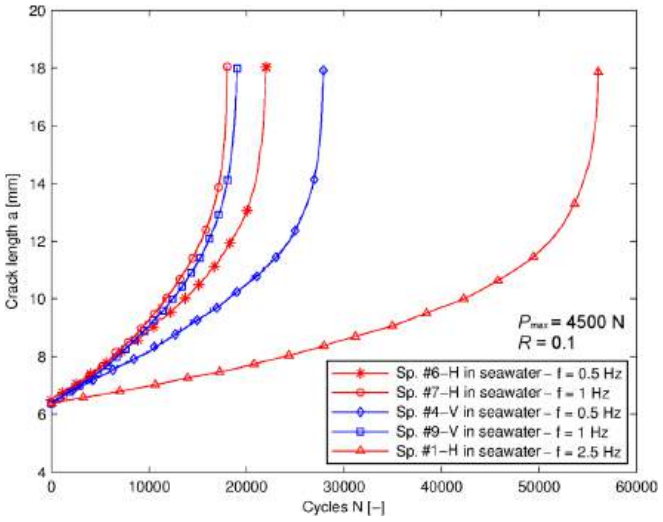

Fig. 9. *a-N* curves for different directions of notch orientation in seawater environment.

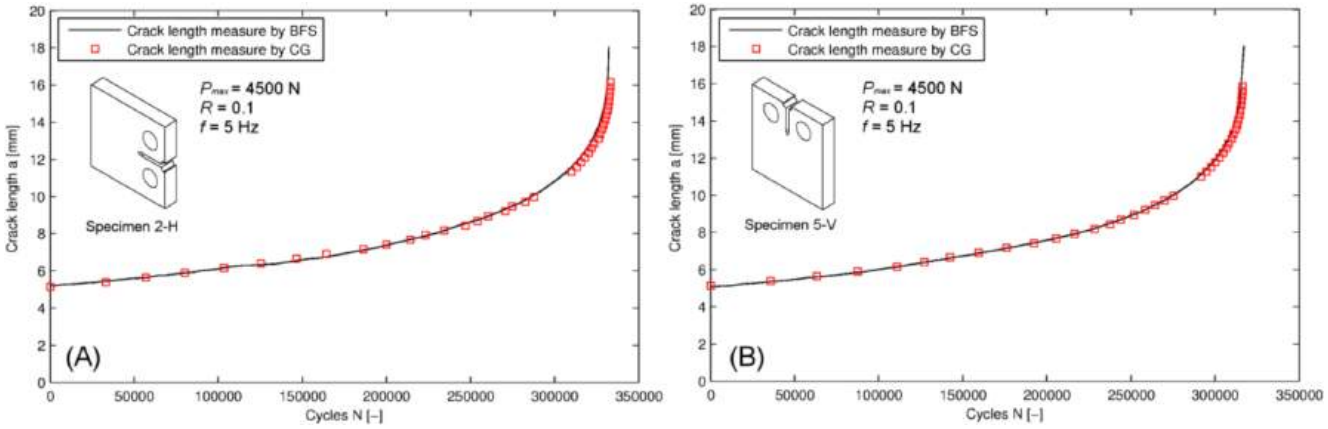

Fig. 7. *a-N* curves obtained by means of data collected by the back-face strain-gauge (black curves) and by the crack-gauges (red squares): (A) specimen n. 2; (B) specimen n. 5.

3.3.2. Experimental results in seawater

The results for the specimens tested in seawater are reported in the current Section. Fig. 9 shows the *a-N* curves after pre-cracking for: specimens n. 7 (red curve with circle scatters, characterized by a H crack) and n. 9 (square scatters with blue curve, characterized by a V crack) at $f = 1$ Hz; specimens n. 4 (diamond scatters with blue curve, V crack) and n. 6 (star scatters with red curve, H crack) at $f = 0.5$ Hz; and specimen n. 1 (triangle scatters with red curve, H crack) at $f = 2.5$ Hz.

From Fig. 9 it can be appreciated that the frequency of loading application does influence the crack growth behaviour. This is mainly due to the fact that the corrosion phenomenon has more time to develop, if the load is applied slowly (*i.e.*, the frequency is lowered). On one hand, this aspect is undoubtedly visible, for example, for specimen n.1 which was tested with the highest frequency (2.5 Hz) after pre-cracking and, therefore, showed the highest fatigue life. On the other hand, the specimens tested with the lowest and the intermediate frequency after pre-cracking (0.5 Hz and 1.0 Hz, respectively) did not show a significant difference. This result is in accordance with the work of Igwemezie *et al.* [47] which reported the crack-growth rate results for marine steels at different frequencies. It was highlighted that higher frequencies lead to a reduction of the growth rate, attributed to reduced corrosion activities due to the limited time provided for the corrosion reaction to effectively occur.

3.3.3. Comparison between experimental results in air and seawater environment

All the obtained *a-N* curves are reported in Fig. 10: black symbols (diamonds, downward triangles, circles, and upward triangles) correspond to tests in air at 5 Hz, while red, blue, and green symbols (diamonds, upward triangles, stars, and squares) denote tests in seawater at different frequencies (0.5 Hz, 1 Hz, and 2.5 Hz).

As aforementioned, on one hand, the black curves, representing specimens tested in air at 5 Hz, show a gradual increase in crack length over a larger number of cycles, indicating a slower crack propagation rate. On the other hand, the red, blue, and green curves show that the crack length in seawater increases more rapidly compared to air, reflecting the more aggressive environment in promoting crack growth. In general, even though there is a small scatter for the test carried out at lower frequencies, 0.5 Hz (shown in red) and 1 Hz (shown in blue), they result in faster crack growth compared to that at the higher frequencies of 2.5 Hz. In any case, the 2.5 Hz crack-growth in seawater (green squares curve), although being the slowest among the seawater conditions, is still faster than the tests conducted in air.

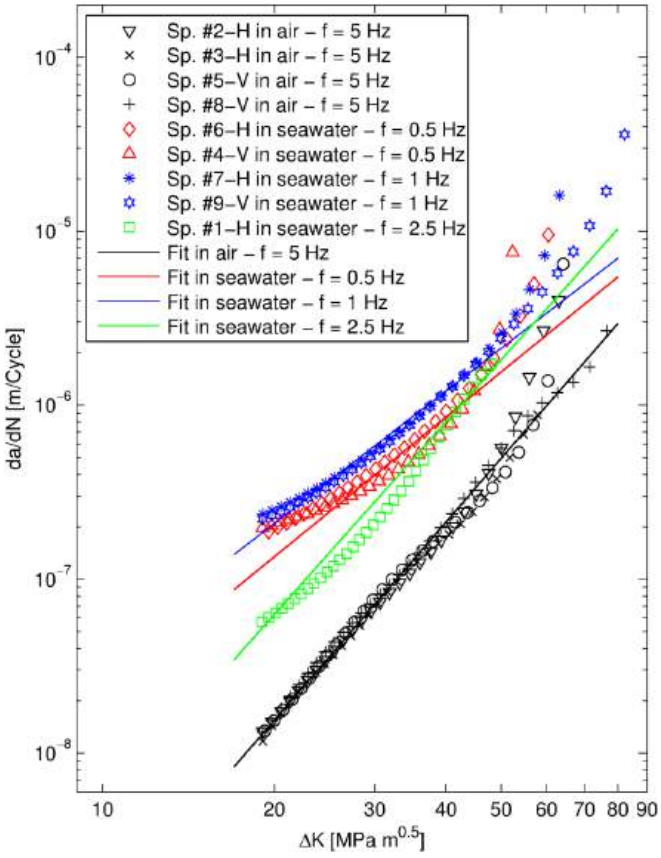

Fig. 11. *da/dN-ΔK* curves for different environment conditions and different loading frequencies.

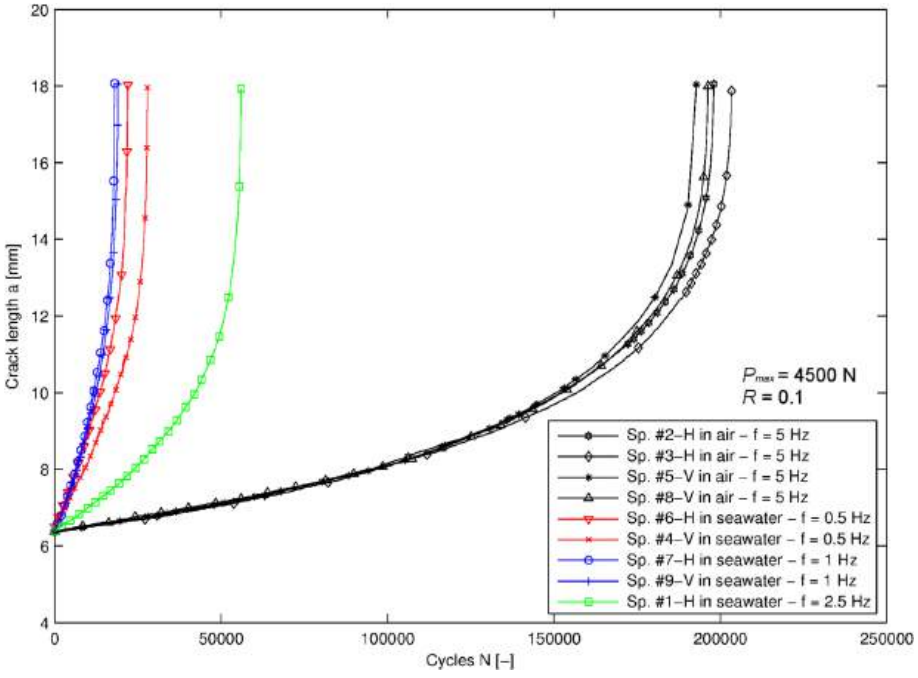

Fig. 10. *a-N* curves for different environment conditions and different loading frequencies.

Fig. 11 shows the crack growth rate (da/dN) versus the stress intensity factor range (ΔK) for the different tested specimens, highlighting the influence of the environment (air *vs.* seawater) and loading frequency (f).

The Eq. (6) reported in ASTM 647 standard [29] was used to determine the stress intensity factor range ΔK:

$$\Delta K = \frac{\Delta P}{B \bullet \sqrt{W}} \bullet \frac{(2+\alpha)}{(1-\alpha)^{3/2}} \bullet \left(0.886 + 4.64 \bullet \alpha + 13.32 \bullet \alpha^2 + 14.72 \bullet \alpha^3 - 5.6 \bullet \alpha^4\right) \quad (6)$$

where:

$\Delta P = (P_{max} - P_{min}) = 4050$ N, $W = 25.4$ mm, $B = 6.65$ mm, $\alpha = a/W$ and a is the crack length.

Moreover, in Fig. 11 are reported the fitting line for each data set that was fitted in Paris region by line with Eq. (7), and the power law constants C and m are reported in Table 5

$$\frac{da}{dN} = C \bullet \Delta K^m \quad (7)$$

In particular: black downward triangles, crosses, circles and pluses represent tests in air at 5 Hz; red diamonds and triangles, blue stars, and green squares represent tests in seawater at varying 0.5 Hz, 1 Hz, and 2.5 Hz, respectively. The black data points generally lie lower, indicating slower crack growth rates compared to those in seawater. The acceleration in short crack growth rates in seawater is attributed to both chemical and microstructural effects. As stated and evaluated in [48,49], aggressive corrosive environments reduce the capability of micro-structural barriers (like, for example, grain boundaries) of impeding the crack growth, thus encouraging the crack growth itself. Indeed, the corrosion at the crack tip generally enhances plasticity, thus lowering the crack growth resistance of the material. In seawater, lower frequencies 0.5 Hz and 1 Hz although with a small scatter tend to show higher crack growth rates compared to higher frequency 2.5 Hz, suggesting that lower loading application speeds amplify the crack growth in corrosive environments, confirming what was already mentioned before.

From Fig. 11, it can be observed that the FCG trends for seawater data fall above the air tests. However, this shift is higher when the tests in seawater are carried out at lower frequency (around 1000 %) compared to the seawater tests at frequency of 2.5 Hz (around 300 %). This confirms that the influence of corrosion on crack growth rate occurs just when the loading frequency is very low. Moreover, for the air test the slope of FCG line is steeper than the seawater tests, though the seawater results always lie above the air ones. Also, in Fig. 11 it is possible to observe that the difference between the crack growth rates in seawater tests and in air is more pronounced for lower value of ΔK respect to higher values of ΔK where this difference is reduced. This is due to the fact that for high crack length, there is not sufficient time for corrosion to help to the crack propagation process and the air results approach the seawater ones. Therefore, it is possible to state that the corrosion damage is more pronounced for lower ΔK, where the crack growth rate is slower, while when the ΔK value increases the corrosion influence is reduced and the fatigue damage prevails.

The same curves are reorganised in Fig. 12A and 12B based on the notch orientation: 'horizontal' along y direction (Fig. 12A) and 'vertical' along x direction (Fig. 12B). In Fig. 12A, the black scatters (inverted triangles and crosses) represent the specimens n. 2 and 3 tested in air, while the red, blue and green scatters represent data for the specimens n. 6, 7 and 1 tested in seawater with a frequency after pre-cracking of 0.5 Hz, 1.0 Hz and 2.5 Hz, respectively.

In Fig. 12B, the black scatters (inverted triangles and crosses) represent the specimens n. 5 and 8 tested in air, respectively, while the red and blue scatters represent data for the specimens n. 4 and 9 tested in seawater with a frequency after pre-cracking of 0.5 Hz and 1.0 Hz, respectively. Both graphs show that specimens tested in seawater generally exhibit higher crack growth rates compared to those tested in air. This indicates the detrimental effect of a corrosive environment on the fatigue properties of 17-4 PH stainless steel. In both air and seawater conditions, specimens tested at lower frequencies tend to have higher crack growth rates. In addition, the results in Fig. 12 confirm that the notch orientation was not a significantly influencing factor, being the notches laying in the same plane and, therefore, sharing the same microstructure. Finally, for an identical value of ΔK, for example $\Delta K = 20$ MPa·m$^{0.5}$, the values of da/dN are reported in Table 6 for comparison. It can be noticed that the crack growth rate could increase, on average, even of almost one order of magnitude in presence of a corrosive environment, respect to the experiments conducted in air. Moreover, focusing on the frequency, the crack growth rate is $6.37 \cdot 10^{-8}$ m/cycle when the testing frequency is 2.5 Hz, while the average value is of $1.83 \cdot 10^{-7}$ m/cycle when the testing frequency is lowered to 0.5 Hz. This again confirms that lower frequencies increase crack propagation rate in corrosion environment.

3.4. Fractographic

The facture surfaces of some C(T) specimens from each environment condition were analysed to understand the crack growth behaviour. Fig. 13A-13D show the fracture surfaces for different lengths of crack for a specimen tested in air environment. The fracture surfaces of the specimens tested in air environment are characterized by transgranular fracture for lower values of $\Delta K = 25.67$ MPa m$^{0.5}$ (Fig. 13A and 13B). In this zone, there are fatigue striations, which are perpendicular to the propagating direction, and secondary cracks. Moreover, in Fig. 13B it is possible to observe lack of fusion defects and un-melted powder particles. Instead, for a higher value of $\Delta K = 45.96$ MPa m$^{0.5}$ (Fig. 13C) the fracture surface becomes a mixture of transgranular and intergranular fracture in fact faceted fracture are present. Finally, a ductile transgranular fracture mode (*i.e.* dimpled rupture) is present (Fig. 13D).

Fig. 13E-13H show the fracture surfaces for different length of crack for a specimen tested in seawater. For specimens tested in seawater, different fracture morphologies were observed. A mixed transgranular and intergranular fracture surface is present for all values of ΔK. The fracture regions for specimens tested in seawater appear slightly smoother, but they share a similar morphology to that of specimens tested in air environment for high values of ΔK, *i.e.* a combination of transgranular (flat facets with striations) and intergranular features. Moreover a brittle fracture mode is present (Fig. 13H). This confirms that in seawater the material is subjected to ion embrittlement that accelerates the crack growth rate.

Table 5
Paris law constants obtained from the tests carried out on 17—4 PH SLM built specimens.

Data set	Environment	P_{max} [N]	R	f [Hz]	C	m	R^2	90 % Confidence Bounds			
								C lower	C upper	m lower	m upper
1	Air	4500	0.1	5	$1.822 \cdot 10^{-13}$	3.789	0.999	$1.822 \cdot 10^{-13}$	$1.822 \cdot 10^{-13}$	3.789	3.789
2	Seawater	4500	0.1	0.5	$4.538 \cdot 10^{-8}$	2.670	0.941	$2.649 \cdot 10^{-8}$	$6.427 \cdot 10^{-8}$	2.556	2.783
3	Seawater	4500	0.1	1.0	$1.075 \cdot 10^{-7}$	2.529	0.992	$9.170 \cdot 10^{-8}$	$1.232 \cdot 10^{-7}$	2.489	2.569
4	Seawater	4500	0.1	2.5	$1.027 \cdot 10^{-9}$	3.680	0.966	$2.819 \cdot 10^{-10}$	$1.771 \cdot 10^{-9}$	3.487	3.874

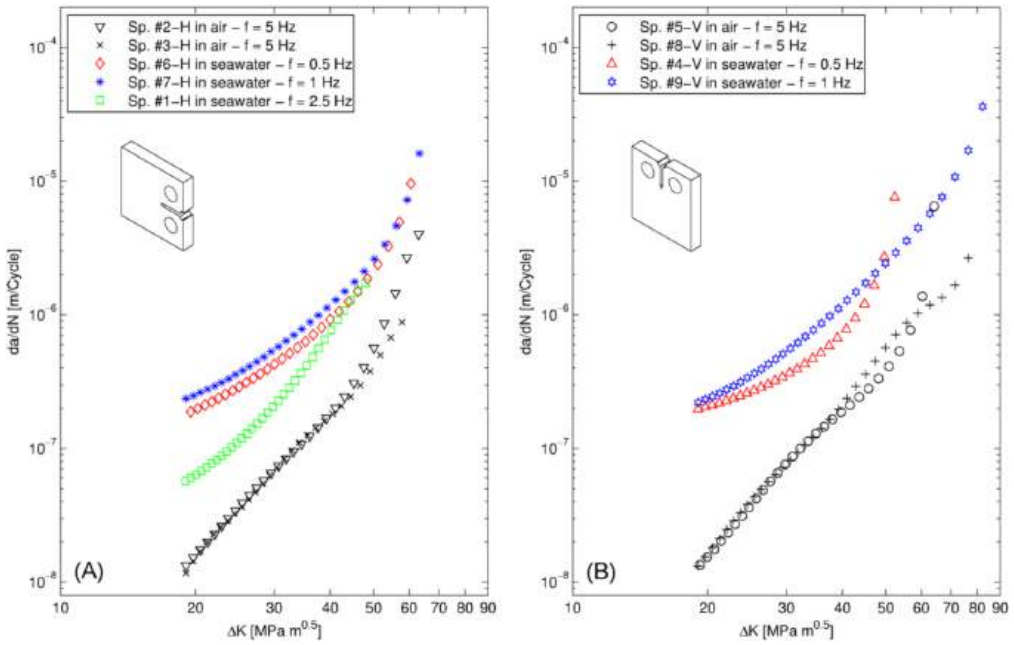

Fig. 12. *da/dN-ΔK* curves for different environment conditions and different loading frequencies: (A) the notch oriented along *y* direction (see Fig. 1); (B) the notch oriented along *x* direction (see Fig. 1).

Table 6
Crack growth rate value for all the tested specimens in correspondence of $\Delta K = 20$ MPa·m$^{0.5}$.

Specimen	Crack direction	Testing environment	Testing freq. after pre-cracking [Hz]	da/*dN* [m/cycle]
2	H	Air	5	$1.59 \cdot 10^{-8}$
3	H	Air	5	$1.52 \cdot 10^{-8}$
5	V	Air	5	$1.54 \cdot 10^{-8}$
8	V	Air	5	$1.64 \cdot 10^{-8}$
6	H	Seawater	0.5	$1.96 \cdot 10^{-7}$
4	V	Seawater	0.5	$1.70 \cdot 10^{-7}$
7	H	Seawater	1	$2.54 \cdot 10^{-7}$
9	V	Seawater	1	$2.38 \cdot 10^{-7}$
1	H	Seawater	2.5	$6.37 \cdot 10^{-8}$

4. Conclusions

The crack-growth behaviour of AM 17-4 PH stainless steel specimens obtained by SLM was investigated in different conditions. Particularly, the C(T) specimens were subjected to metallographic analyses, instrumented and tested both in air and in a corrosive environment resembling seawater. The crack-growth experiments carried out under corrosion considered different load frequencies in order to quantify their impact on the corrosion cracking phenomenon. The following observations were highlighted from the analyses conducted so far:

- the microstructure is characterised by the laser scanning path with circular patterns indicating the SLM process profiles and by the epitaxial grains grown in the build direction;
- the corrosion characteristics of the material, evaluated through OCP and PD curves, are in accordance with those available in literature for the same material obtained with the same manufacturing process;
- the fatigue crack-growth behaviour of the material is highly dependent on the environment (air *vs.* seawater). The crack growth rate increased, on average, even of almost one order of magnitude in presence of a corrosive environment, respect to the experiments conducted in air;
- the crack-growth is susceptible to the frequency of loading. Lower loading frequencies sensibly increase the fatigue crack growth rate, due to the longer time the corrosion phenomenon has to develop and occur;
- for specimens tested in seawater environment, a mixed transgranular and intergranular fracture surface is present for all values of *ΔK*. This confirms that in seawater the material is subjected to ion embrittlement that accelerates the crack growth rate.

The novelty of this study lies in the combined analysis of load frequency and environmental conditions on corrosion fatigue of SLM 17-4 PH steel – a topic that remains relatively new in literature. The identification of a strong frequency-dependent crack growth acceleration in corrosive environments provides valuable insight into the durability and damage mechanisms of additively manufactured components. As SLM is being increasingly adopted as manufacturing technique for components to be used in critical structural applications in marine, aerospace, and energy sectors, understanding its behaviour in harsh conditions is essential.

Near-future developments will involve experiments on traditionally rolled 17-4 PH stainless steel specimens to serve as a reference for understanding the specific impact of the SLM process on corrosion fatigue performance. The scientific hypothesis guiding this follow-up research is that the manufacturing process, particularly the microstructural features introduced by SLM, plays a significant role in determining the material's sensitivity to corrosion-assisted fatigue. The aim is to verify whether the increased crack-growth rates and fracture mechanisms observed in SLM specimens under corrosive environments are also present in traditional rolled specimens under identical testing conditions. This will help to determine: i) if SLM-induced microstructural features (e.g., epitaxial grain growth, residual stresses, process-induced defects) accelerate corrosion fatigue compared to rolled microstructures, which are typically more homogeneous; ii) if the same frequency-dependent corrosion behaviour observed in SLM specimens is evident for rolled ones, as well, or if the latter exhibit a less pronounced sensitivity.

However, the main issue with 17-4 PH stainless steel is that the precipitation happening during the heat cycles/treatments clearly influences the microstructure formation. For this reason, it is clear that different heating cycles/treatments could lead to differently characterized microstructures. Therefore, tuning both the SLM process and the traditional rolling in order to get two materials with comparable

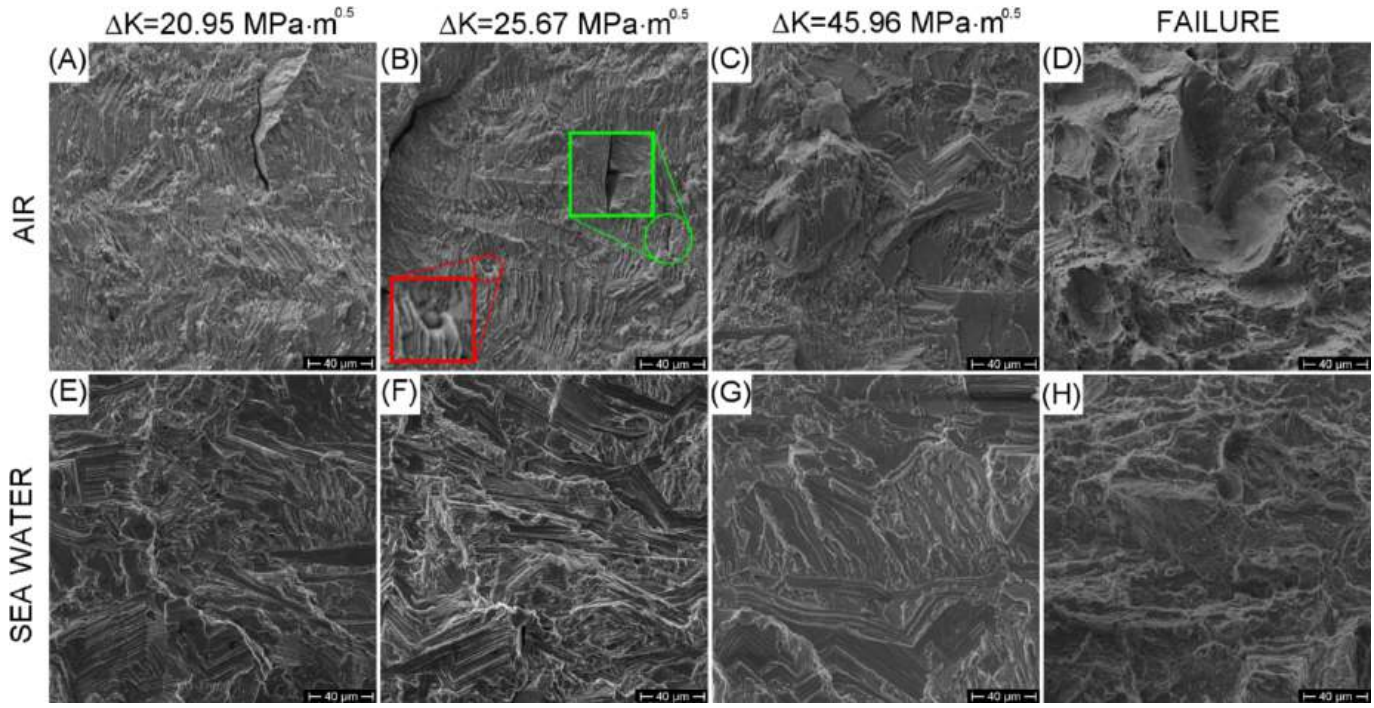

Fig. 13. SEM scans of the fracture specimen: (A-D) specimen tested in air environment; (E-H) specimen tested in seawater environment.

microstructures is not an easy task but it is mandatory for carrying out a reliable and robust comparison. In conclusion, a future comparative study will allow to assess the reliability of additively manufactured parts relative to conventionally produced ones in service environments where corrosion fatigue is a concern. It may also inform the development of post-processing or design strategies to mitigate the observed drawbacks in SLM materials.

CRediT authorship contribution statement

America Califano: Writing – review & editing, Writing – original draft, Methodology, Investigation, Formal analysis, Data curation, Conceptualization. **Enrico Armentani:** Writing – review & editing, Supervision, Conceptualization. **Filippo Berto:** Writing – review & editing, Supervision, Methodology. **Raffaele Sepe:** Writing – review & editing, Validation, Supervision, Methodology, Investigation, Formal analysis, Data curation, Conceptualization.

Declaration of competing interest

The authors declare that they have no known competing financial interests or personal relationships that could have appeared to influence the work reported in this paper.

Data availability

Data will be made available on request.

References

[1] Giannella V. Uncertainty quantification in fatigue crack-growth predictions. Int J Fract 2022;235:179–95. https://doi.org/10.1007/s10704-022-00624-4.
[2] Ko G, Kim W, Kwon K, Lee TK. The corrosion of stainless steel made by additive manufacturing: a review. Metals (Basel) 2021;11:1–21. https://doi.org/10.3390/met11030516.
[3] Thorpe TW, Scott PM, Rance A, Silvester D. Corrosion fatigue of BS 4360:50D structural steel in seawater. 1983.
[4] Afkhami S, Dabiri M, Alavi SH, Björk T, Salminen A. Fatigue characteristics of steels manufactured by selective laser melting. Int J Fatigue 2019;122:72–83. https://doi.org/10.1016/J.IJFATIGUE.2018.12.029.
[5] Citarella R, Giannella V. Additive Manufacturing in Industry. Applied Sciences 2021, Vol 11, Page 840 2021;11:840. doi: 10.3390/APP11020840.
[6] Gibson I, Rosen D, Stucker B, Khorasani M. Additive manufacturing technologies. Springer Nature Switzerland AG 2021. https://doi.org/10.1007/978-3-030-56127-7.
[7] Alfieri V, Giannella V, Caiazzo F, Sepe R. Influence of position and building orientation on the static properties of LPBF specimens in 17-4 PH stainless steel. Forces Mech 2022;8. https://doi.org/10.1016/J.FINMEC.2022.100108.
[8] Sepe R, De Luca A, Giannella V, Borrelli R, Franchitti S, Di Caprio F, et al. Influence of dimension, building position, and orientation on mechanical properties of EBM lattice Ti6Al4V trusses. Int J Adv Manuf Technol 2022;122:3183–98. https://doi.org/10.1007/S00170-022-10051-3.
[9] Sepe R, Franchitti S, Borrelli R, Di Caprio F, Armentani E, Caputo F. Correlation between real geometry and tensile mechanical behaviour for Ti6Al4V electron beam melted thin specimens. Theor Appl Fract Mech 2020;107:102519. https://doi.org/10.1016/j.tafmec.2020.102519.
[10] De Luca A, Lamanna G, Caputo F, Borrelli R, Franchitti S, Pirozzi C, et al. Effects of the surface finish on thin specimens made by electron beam melting technology. Macromol Symp 2021;396. https://doi.org/10.1002/MASY.202000307.
[11] Sepe R, Giannella V, Alfieri V, Caiazzo F. Static and fatigue behavior of laser welded additively manufactured 17-4 PH steel plates. Procedia Struct Integrity 2021;34:172–7. https://doi.org/10.1016/J.PROSTR.2021.12.025.
[12] Foti P, Mohammad Javad Razavi S, Fatemi A, Berto F. Multiaxial fatigue of additively manufactured metallic components: a review of the failure mechanisms and fatigue life prediction methodologies. Prog Mater Sci 2023;137:101126. https://doi.org/10.1016/J.PMATSCI.2023.101126.
[13] Karakaş Ö, Kardeş FB, Foti P, Berto F. An overview of factors affecting high-cycle fatigue of additive manufacturing metals. Fatigue Fract Eng Mater Struct 2023;46:1649–68. https://doi.org/10.1111/FFE.13967.
[14] Malakshah MG, Eslami A, Ashrafizadeh F, Berenjkoub A. Effect of heat treatment on corrosion, fatigue, and corrosion fatigue behavior of 17-4PH stainless steel. J Mater Eng Perform 2023;32:6610–21. https://doi.org/10.1007/s11665-022-07614-6.
[15] Wu M, Zhao Z, Wang X, Wang C, Liang P. Corrosion behavior of PH stainless steel in simulated marine environment. Mater Corros 2019;70:461–9. https://doi.org/10.1002/maco.201810454.
[16] Peng D, Jones R, Berto F, Razavi SMJ. Effect of corrosion and fatigue on the remaining life of structures and its implication to additive manufacturing. Frattura e Integrità Strutturale 2018;45:33–44. https://doi.org/10.3221/IGF-ESIS.45.03.
[17] Neuber H. Theory of notch stresses. Mater Corros 1985;36:307.
[18] Hemmasian Ettefagh A, Guo S, Raush J. Corrosion performance of additively manufactured stainless steel parts: a review. Addit Manuf 2021;37. https://doi.org/10.1016/j.addma.2020.101689.
[19] Baragetti S, Villa F. SCC and Corrosion Fatigue characterization of a Ti-6Al-4V alloy in a corrosive environment – experiments and numerical models. Frattura e Integrità Strutturale 2014;30:84–94. https://doi.org/10.3221/IGF-ESIS.30.12.
[20] Stoudt MR, Ricker RE, Lass EA, Levine LE. Influence of postbuild microstructure on the electrochemical behavior of additively manufactured 17-4 ph stainless steel. JOM 2017;69:506–15. https://doi.org/10.1007/s11837-016-2237-y.

[21] Syrett BC, Viswanathan R, Wing SS, Wittig JE. Effect of Microstructure on Pitting and Corrosion Fatigue of 17-4 PH Turbine Blade Steel in Chloride Environments*. vol. 35. The Electrochem. Soc., Inc; 1979.
[22] Califano A, Bollino F, Berto F, Sepe R. Experimental investigation of the fatigue crack growth behaviour in SLM additively manufactured 17-4 PH stainless steel specimens. Procedia Structural Integrity, vol. 48, Elsevier B.V.; 2023, p. 238–43. doi: 10.1016/j.prostr.2023.07.154.
[23] Califano A, Bollino F, Berto F, Raffaele S. Fatigue crack-growth behavior of wrought and additively manufactured 17 - 4 PH stainless steel specimens. Procedia Structural Integrity, vol. 53, Elsevier B.V.; 2024, p. 185–9. doi: 10.1016/j.prostr.2024.01.023.
[24] Shojai S, Schaumann P, Braun M, Ehlers S. Influence of pitting corrosion on the fatigue strength of offshore steel structures based on 3D surface scans. Int J Fatigue 2022;164. https://doi.org/10.1016/j.ijfatigue.2022.107128.
[25] Schönbauer BM, Stanzl-Tschegg SE, Perlega A, Salzman RN, Rieger NF, Turnbull A, et al. The influence of corrosion pits on the fatigue life of 17-4PH steam turbine blade steel. Eng Fract Mech 2015;147:158–75. https://doi.org/10.1016/j.engfracmech.2015.08.011.
[26] Caiazzo F, Alfieri V. Optimization of laser beam welding of steel parts made by additive manufacturing. Int J Adv Manuf Technol 2021;114:3123–36. https://doi.org/10.1007/S00170-021-07039-W/TABLES/13.
[27] Califano A, Bollino F, Berto F, Sepe R. Experimental investigation of the fatigue crack growth behaviour in SLM additively manufactured 17-4 PH stainless steel specimens. Procedia Struct Integrity 2023;48:238–43. https://doi.org/10.1016/J.PROSTR.2023.07.154.
[28] EOS StainlessSteel GP1 for EOSINT M 270. n.d.
[29] ASTM D1141-98 - Standard Practice for the Preparation of Substitute Ocean Water. 2021.
[30] ASTM 647 - Test Method for Measurement of Fatigue Crack Growth Rates 2023. doi: 10.1520/E0647-23A.
[31] Newman JC, Yamada Y, James MA. Back-face strain compliance relation for compact specimens for wide range in crack lengths. Eng Fract Mech 2011;78:2707–11. https://doi.org/10.1016/j.engfracmech.2011.07.001.
[32] Aripin MA, Sajuri Z, Jamadon NH, Baghdadi AH, Mohamed IF, Syarif J, et al. Microstructure and mechanical properties of selective laser melted PH stainless steel; Build direction and heat treatment processes. Mater Today Commun 2023;36. https://doi.org/10.1016/j.mtcomm.2023.106479.
[33] Nezhadfar PD, Burford E, Anderson-Wedge K, Zhang B, Shao S, Daniewicz SR, et al. Fatigue crack growth behavior of additively manufactured 17-4 PH stainless steel: Effects of build orientation and microstructure. Int J Fatigue 2019;123:168–79. https://doi.org/10.1016/j.ijfatigue.2019.02.015.
[34] Alnajjar M, Christien F, Wolski K, Bosch C. Evidence of austenite by-passing in a stainless steel obtained from laser melting additive manufacturing. Addit Manuf 2019;25:187–95. https://doi.org/10.1016/j.addma.2018.11.004.
[35] Shifeng W, Shuai L, Qingsong W, Yan C, Sheng Z, Yusheng S. Effect of molten pool boundaries on the mechanical properties of selective laser melting parts. J Mater Process Technol 2014;214:2660–7. https://doi.org/10.1016/j.jmatprotec.2014.06.002.
[36] Cheruvathur S, Lass EA, Campbell CE. Additive manufacturing of 17-4 PH STAINLESS STEEL: POST-PROCESSING HEAT TREATMENT TO ACHIEVE UNIFORM REPRODUCIBLE MICROSTRUCTure. JOM 2016;68:930–42. https://doi.org/10.1007/s11837-015-1754-4.
[37] Meredith SD, Zuback JS, Keist JS, Palmer TA. Impact of composition on the heat treatment response of additively manufactured PH grade stainless steel. Mater Sci Eng A 2018;738:44–56. https://doi.org/10.1016/j.msea.2018.09.066.
[38] Sabooni S, Chabok A, Feng SC, Blaauw H, Pijper TC, Yang HJ, et al. Laser powder bed fusion of PH stainless steel: A comparative study on the effect of heat treatment on the microstructure evolution and mechanical properties. Addit Manuf 2021;46. https://doi.org/10.1016/j.addma.2021.102176.
[39] Liu W, Ma J, Atabaki MM, Pillai R, Kumar B, Vasudevan U, et al. Hybrid laser-arc welding of 17-4 PH martensitic stainless steel. Lasers Manuf Mater Process 2015;2:74–90. https://doi.org/10.1007/s40516-015-0007-2.
[40] Coulson S. Analysis of Additively Manufactured 17-4PH Stainless Steel. n.d.
[41] Hsiao CN, Chiou CS, Yang JR. Aging reactions in a 17-4 PH stainless steel. vol. 74. 2002.
[42] Clausen B, Brown DW, Carpenter JS, Clarke KD, Clarke AJ, Vogel SC, et al. Deformation behavior of additively manufactured GP1 stainless steel. Mater Sci Eng A 2017;696:331–40. https://doi.org/10.1016/j.msea.2017.04.081.
[43] LeBrun T, Nakamoto T, Horikawa K, Kobayashi H. Effect of retained austenite on subsequent thermal processing and resultant mechanical properties of selective laser melted 17-4 PH stainless steel. Mater Des 2015;81:44–53. https://doi.org/10.1016/j.matdes.2015.05.026.
[44] Irrinki H, harper T, Badwe S, Jason S, Gulsoy O, Gupta G, et al. Effects of powder characteristics and processing conditions on the corrosion performance of 17-4 PH stainless steel fabricated by laser-powder bed fusion. Progress in Additive Manufacturing 2018:39–49. doi: doi: 10.1007/s40964-018-0048-0.
[45] Forcellese P, Belegni S, Silvi A, Mancia T, Simoncini M, Bellezze T. Study of corrosion resistance of 17-4 PH stainless steel as-sintered and heat-treated samples manufactured by Bound Metal Deposition TM. n.d.
[46] Yadollahi A, Shamsaei N, Thompson SM, Elwany A, Bian L. Effects of building orientation and heat treatment on fatigue behavior of selective laser melted 17-4 PH stainless steel. Int J Fatigue 2017;94:218–35. https://doi.org/10.1016/j.ijfatigue.2016.03.014.
[47] Igwemezie V, Mehmanparast A. Waveform and frequency effects on corrosion-fatigue crack growth behaviour in modern marine steels. Int J Fatigue 2020;134. https://doi.org/10.1016/j.ijfatigue.2020.105484.
[48] Murtaza G, Akidt R. Corrosion fatigue short crack growth behaviour in a high strength steel. 1996.
[49] Saeed H, Chaudhuri S, De Waele W. Experimental evaluation of the short and long fatigue crack growth rate of S355 structural steel offshore monopile weldments in air and synthetic seawater. Appl Ocean Res 2024;149. https://doi.org/10.1016/j.apor.2024.104063.